Structural Characterization of CeO₂−MO₂ (M = Si⁴⁺, Ti⁴⁺, and Zr⁴⁺) Mixed Oxides by Raman Spectroscopy, X-ray Photoelectron Spectroscopy, and Other Techniques

Benjaram M. Reddy* and Ataullah Khan

Inorganic and Physical Chemistry Division, Indian Institute of Chemical Technology,
Hyderabad 500 007, India

Yusuke Yamada and Tetsuhiko Kobayashi

National Institute of Advanced Industrial Science and Technology (AIST),
Special Division of Green Life Technology, 1-8-31 Midorigaoka, Ikeda, Osaka 563-8577, Japan

Stéphane Loridant and Jean-Claude Volta

Institut de Recherches sur la Catalyse−CNRS, 2 Avenue A. Einstein, 69626 Villeurbanne Cedex, France

Microstructure evolution of ceria-based mixed oxides CeO₂−MO₂ (M = Si⁴⁺, Ti⁴⁺, and Zr⁴⁺) after thermal treatments in the temperature range of 773−1073 K were investigated by X-ray diffraction (XRD), Raman spectroscopy, X-ray photoelectron spectroscopy (XPS), and other techniques. The CeO₂−SiO₂ was synthesized by a deposition precipitation method, and a coprecipitation procedure was adopted to make CeO₂−TiO₂ and CeO₂−ZrO₂ binary oxides. The XRD measurements revealed the presence of crystalline cubic CeO₂ on the surface of SiO₂ in CeO₂−SiO₂, CeO₂ and TiO₂ (anatase) in CeO₂−TiO₂, and Ce₀.₇₅Zr₀.₂₅O₂ and Ce₀.₆Zr₀.₄O₂ phases in CeO₂−ZrO₂ samples. The crystallinity of these phases increased as the calcination temperature increased. Estimations of the cell parameter *a* indicated an expansion of the CeO₂ lattice in the case of CeO₂−TiO₂ samples, whereas a contraction was noted in the case of CeO₂−ZrO₂. Some incorporation of Si⁴⁺ ions into the CeO₂ lattice was noted at higher calcination temperatures for the CeO₂−SiO₂ samples. Raman measurements revealed the presence of oxygen vacancies, lattice defects, and the displacement of oxide ions from their normal lattice positions in the case of the CeO₂−TiO₂ and CeO₂−ZrO₂ samples. The XPS studies revealed the presence of silica, titania, and zirconia in their highest oxidation states—Si⁴⁺, Ti⁴⁺, and Zr⁴⁺—at the surface of the materials. Cerium is present in both Ce⁴⁺ and Ce³⁺ oxidation states, but in different proportions, depending on the mixed-oxide system and the calcination temperature used.

1. Introduction

There are several emerging catalytic processes for which cerium oxide is being actively investigated. It forms an integral part of three-way catalysts and serves as a promoter to the commercial fluid catalytic cracking (FCC) catalysts. Other significant applications of cerium oxide-based materials include use in oxygen permeation membrane systems, fuel cell processes, catalytic wet oxidation, and exhaust combustion catalysts.[1−10] Recently, it also has been used in the deNOx catalysis.[11] The success of ceria (CeO₂) is mainly due to its unique combination of an elevated oxygen transport capacity coupled with the ability to shift easily between reduced and oxidized states (Ce³⁺ ↔ Ce⁴⁺).[9] Nevertheless, the major drawback of an oxygen storage system based on pure CeO₂ is related to its thermal resistance, low-temperature activity, and textural stability, which are not high enough to meet the requirements of high-temperature applications.[12] Therefore, much effort has been directed recently to find catalyst formulations that can enhance the thermal (textural) stability of CeO₂ without diminishing its special features, such as its unique redox properties and its high oxygen mobility. The preparation of

compounds or solid solutions with many rare-earth elements and transition metals has been attempted to overcome some of the previously mentioned disabilities of CeO₂.[13]

CeO₂ easily forms solid solutions with other rare-earth elements and with elements belonging to the transition-metal series. Among rare-earth elements, CeO₂−Ln₂O₃ (Ln = La, Pr, Sm, Gd, and Tb) systems have been extensively investigated and their effects have been closely monitored.[9,14−16] Regarding transition/nontransition elements, CeO₂ easily forms solutions with ZrO₂,[17,18] PbO₂,[19] CuO,[20] MnOₓ,[21] TiO₂,[22,23] Al₂O₃,[24] and SiO₂,[25−27] and each has its own uniqueness. The ability to substitute one cation for another in a particular structure is dependent on several factors, such as the dimensions of the host/guest cation and the structural features of the pure oxide.[13] During the formation of mixed-oxide phases, the structural and energetic factors of the individual constituents are profoundly modified. The resulting redox, catalytic, and thermal properties can be very different from those of pure oxides.[28] When designing CeO₂-based mixed oxides, several factors must be considered,[9] such as the effect of dopant concentration (a high concentration of ions with redox character is generally preferred) and the presence of a single phase (a fluorite-structured material is favored). The host/guest cation should preferably induce stress and structural defects, because of the difference in the ionic

* Author to whom correspsondence should be addressed. E-mail: bmreddy@iict.ap.nic.in, mreddyb@yahoo.com.

radius between cations. Therefore, an effort has been made in the present study to understand the evolution of CeO_2-SiO_2, CeO_2-TiO_2, and CeO_2-ZrO_2 mixed oxides of great commercial significance. Accordingly, a 1:1 molar ratio of CeO_2-MO_2 binary oxides (M = Si^{4+}, Ti^{4+}, and Zr^{4+}) were synthesized by adopting a deposition precipitation (CeO_2-SiO_2) or coprecipitation (CeO_2-TiO_2 and CeO_2-ZrO_2) methodology. The obtained samples were subjected to thermal treatments over the temperature range of 773–1073 K and were investigated by means of X-ray diffraction (XRD), Raman spectroscopy (RS), X-ray photoelectron spectroscopy (XPS), Brunauer–Emmett–Teller (BET) surface area, and thermal techniques (thermogravimetric analysis/differential thermal analysis (TGA/DTA)).

2. Experimental Section

2.1. Preparation of Samples. The CeO_2-TiO_2 and CeO_2-ZrO_2 binary oxides (1:1 molar ratio, based on oxides) were prepared by a coprecipitation method. The precursors used in the preparation of CeO_2-TiO_2 were $CeCl_3 \cdot 7H_2O$ (99.0%, Aldrich) and $TiCl_4$ (99.9%, Aldrich), whereas ammonium cerium(IV) nitrate (Loba Chemie, GR grade) and zirconium(IV) nitrate (Fluka, AR grade) were used in the preparation of CeO_2-ZrO_2. In a typical experiment, requisite quantities of the precursors were dissolved in double-distilled water and mixed together. To make titanium chloride solution, the $TiCl_4$ was first digested in cold concentrated HCl and then diluted with distilled water. Dilute ammonia was added gradually dropwise to the aforementioned mixture solution (pH = 2), with vigorous stirring, until the precipitation was complete (pH = 8). The obtained precipitate was filtered off and washed several times with double-distilled water until it was free from Cl^- ions. The obtained cake was oven-dried at 393 K for 12 h and finally calcined at 773 K for 5 h. Some portions of the calcined mixed oxides were once again heated at 873, 973, and 1073 K for 5 h.

The CeO_2-SiO_2 mixed oxide (1:1 molar ratio, based on oxides) was prepared by a deposition precipitation method. In a typical experiment, the requisite quantities of ammonium cerium(IV) nitrate (Loba Chemie, GR grade), dissolved separately in deionized water, and colloidal silica (40 wt %, Fluka, AR grade) were mixed together. Dilute aqueous ammonia solution was gradually added dropwise to the aforementioned mixture solution, with vigorous stirring, until the precipitation was complete (pH = 8). The resulting product was filtered off, washed with distilled water, oven-dried at 383 K for 12 h, and then calcined at 773 K for 5 h in an air atmosphere. Some portions of this calcined support were once again heated at 873, 973, and 1073 K for 5 h in a closed electrical furnace in an air atmosphere. The rate of heating, as well cooling, was always maintained at 10 K/min. In all these preparations, the mass balance was thoroughly scrutinized to ensure that no losses in weight of the obtained products from the precursors occurred.

2.2. Characterization of Samples. The TGA/DTA curves were obtained on a Mettler Toledo TG-SDTA apparatus. The sample was heated from ambient temperature to 1173 K under a nitrogen flow. The sample weight was ca. 12 mg, and the heating rate was 10 K/min.

The BET surface areas were determined by N_2 adsorption, using a Micromeritics Gemini 2360 instrument. Prior to analysis, the samples were oven-dried at 393 K for 12 h and flushed with argon gas for 2 h.

Powder X-ray diffraction (XRD) patterns were recorded on a Siemens D-500 diffractometer, using a nickel-filtered Cu Kα (0.15418 nm) radiation source. The intensity data were collected over a 2θ range of 3°–80°, with a 0.02° step size and using a counting time of 1 s per point. Crystalline phases were identified by comparison with the reference data from International Centre for Diffraction Data (ICDD) files. The average crystallite size of CeO_2 was estimated with the help of the Debye–Scherrer equation, using the XRD data of all prominent lines.[29] The cell parameter *a* values were calculated by a standard cubic indexation method, using the intensity of the CeO_2 base peak (111).[30,31]

The Raman spectra were obtained on a DILOR XY spectrometer that was equipped with a liquid-nitrogen cooled charge-coupled device (CCD) detector. The emission line at 514.5 nm from an Ar^+ ion laser (Spectra Physics) was focused on the sample under a microscope, and width of the analyzed spot was ~1 μm. The power of the incident beam on the sample was 3 mW. Time of acquisition was adjusted according to the intensity of the Raman scattering. The wavenumber values reported from the spectra are accurate to within 2 cm^{-1}. For each solid, the spectra were recorded at several points of the sample (more than six), to ascertain the homogeneity of the sample, and the average of all these spectra were plotted in the figure presented in this study.

The XPS measurements were performed on a Shimadzu (ESCA 3400) spectrometer using Mg Kα (1253.6 eV) radiation as the excitation source. Charging of the catalyst samples was corrected by setting the binding energy of the adventitious carbon (C 1s) at 284.6 eV.[32,33] The XPS analysis was performed at ambient temperature and at pressures typically on the order of $<10^{-6}$ Pa. Prior to analysis, the samples were outgassed in a vacuum oven overnight. Quantitative analysis of atomic ratios was accomplished by determining the elemental peak areas, following the Shirly background subtraction by the usual procedures documented in the literature.[32,33]

3. Results and Discussion

The as-synthesized CeO_2-MO_2 (M = Si^{4+}, Ti^{4+}, and Zr^{4+}) mixed oxides were subjected to TGA/DTA analysis before calcination. The obtained thermograms, in the range of 273–1173 K and at a ramp of 10 K/min, are shown in Figure 1. These thermograms, in general, reveal one major and two minor weight-loss peaks. The TGA profile of the CeO_2-TiO_2 sample is slightly different in the peak maxima temperature regions from other two samples. The first major low-temperature peak in the 309–463 K range is primarily due to the loss of nondissociative adsorbed water, as well as water held on the surface by hydrogen bonding. The second minor weight-loss peak could be due to loss of water held in the micropores of the mixed oxide gel. A further loss of water occurs at slightly higher temperatures, because of dehydroxylation of the surface. In the case of the CeO_2-SiO_2 sample, the weight loss from ambient to 470 K is ~10% and from 470 K to 723 K is 5%. However, the weight loss between 723 and 1073 K is only ~1%, which indicates that, over the temperature range of 723–1073 K, the CeO_2-SiO_2 binary oxide is quite stable, in terms of phases and chemical composition. In the case of CeO_2-TiO_2, the loss of sample weight from ambient to 735 K is ~11% and from 735 to 1273 K is ~0.4%. Thus, in the range of 735–1273 K, the CeO_2-TiO_2 binary oxide seems to be thermally quite stable. A weight loss of ~23% is observed in the case of the CeO_2-ZrO_2 sample from ambient to 926 K, and, thereafter, a small loss of 0.6% was observed from 926 to 1273 K. The thermodynamically feasible transformation of $Ce_{0.75}Zr_{0.25}O_2$ to $Ce_{0.6}Zr_{0.4}O_2$ was expected at ~873 K, according to the DTA plot of this sample.[4]

Structural Characterization of CeO₂−MO₂ Mixed Oxides

J. Phys. Chem. B, Vol. 107, No. 41, 2003 **11477**
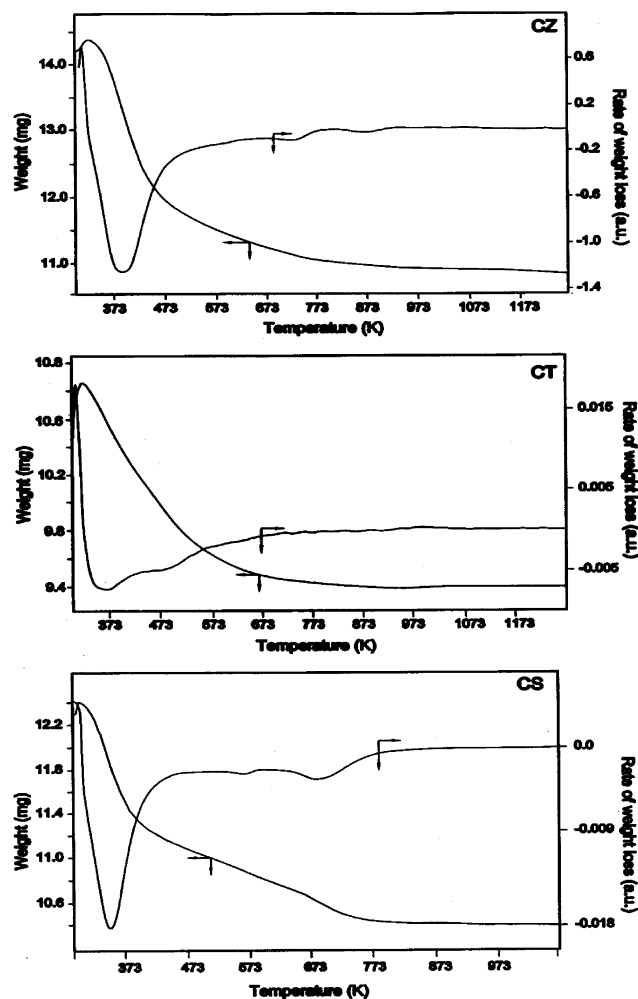

Figure 1. TGA/DTA profiles of various CeO₂−MO₂ (M = Si⁴⁺ (CeO₂−SiO₂, CS), Ti⁴⁺ (CeO₂−TiO₂, CT), and Zr⁴⁺ (CeO₂−ZrO₂, CZ)) binary oxides before calcinations.

Figure 2. Powder X-ray diffraction (XRD) patterns of various CeO₂−MO₂ (M = (a) Si⁴⁺ (CS), (b) Ti⁴⁺ (CT), and (c) Zr⁴⁺ (CZ)) binary oxides calcined at different temperatures. Peak legend is as follows: (*) lines due to CeO₂, (■) lines due to Ce₀.₇₅Zr₀.₂₅O₂, (#) lines due to Ce₀.₆Zr₀.₄O₂, and (+) lines due to TiO₂ anatase.

The powder XRD patterns of various mixed oxides calcined at different temperatures in the range of 773−1073 K were recorded under ambient conditions. The XRD profiles of the samples calcined at 773 and 1073 K are shown in Figure 2. As can be noted from this figure, the CeO₂−SiO₂ mixed oxide (the CS plot in Figure 2a) calcined at 773 K exhibits poor crystallinity. Only the broad diffraction lines due to CeO₂ (ICDD PDF No. 34-0394) could be observed. With increasing calcination temperature from 773 K to 1073 K, a gradual increase in the intensity of the lines due to better crystallization of cerium oxide was noted. Another observation to be mentioned from XRD measurements is that there are no extra lines due to compounds or mixed phases between CeO₂ and SiO₂. Recently, Rocchini et al. investigated the CeO₂−SiO₂ combination (co-precipitation) and attributed the enhanced textural and thermal stability of these mixed oxides to the formation of an intermediate Ce₉.₃₃(SiO₄)₆O₂ (characterized by TEM and XRD) phase between CeO₂ and SiO₂, which, on suitable treatment, decomposes to amorphous silica and smaller crystallites of CeO₂.[13,34,35] In the present study, there is no evidence for the formation of such compound between CeO₂ and SiO₂, which can be attributed to a different preparation method that is adopted and the calcination temperature that is used.

The powder XRD patterns of the CeO₂−TiO₂ binary oxide calcined at 773 and 1073 K are shown in Figure 2b (in the CT plot). The XRD measurements provide typical diffraction patterns of cubic CeO₂ (ICDD PDF No. 34-0394), along with
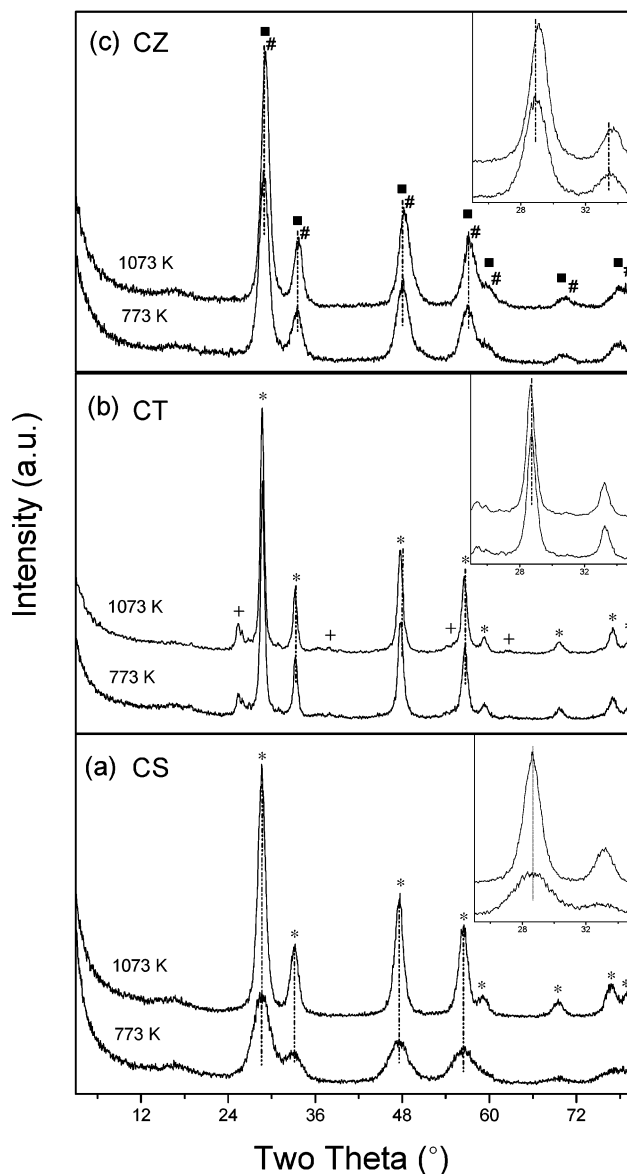
few less-intense peaks due to the TiO₂ (anatase) phase (ICDD PDF No. 21-1272). With increasing calcination temperature, a slight increase in the intensity of the lines due to both these phases was observed. Preuss and Gruehn reported various Ce-Ti-O oxides—namely, Ce₂TiO₅, Ce₂Ti₂O₇, and Ce₄Ti₉O₂₄—by heating the appropriate mixtures of solids that contained cerium and titanium at 1523 K.[28] However, no such crystalline phases could be observed in the present study for which calcination was limited at 1073 K. The absence of crystalline Ce-Ti-O compounds may be due to a different preparation method that was adopted and lower calcination temperatures that were used in the present investigation. It is an established fact in the literature that the transformation of anatase to rutile is thermodynamically feasible at temperatures of >873 K in impurity-free TiO₂ samples.[36] However, there is no evidence regarding the formation of a rutile phase, even up to 1073 K, in the present study. Apparently, the anatase-to-rutile phase transformation is somehow inhibited in the CeO₂−TiO₂ mixed-oxide system. As explained by Lin and Yu, this phenomenon could be due to

11478 *J. Phys. Chem. B, Vol. 107, No. 41, 2003*

Reddy et al.

stabilization of the anatase by the surrounding Ce ions through the formation of Ce-O-Ti bonds.[37] At the interface, Ti atoms are expected to substitute for Ce atoms in the lattice of the cerium oxide to form octahedral Ti sites. The interaction between the tetrahedral Ti and octahedral Ti sites inhibits the anatase phase transformation to rutile.[36] Anderson and Bard also offered an analogous explanation for TiO_2-SiO_2 mixed oxides where similar inhibition of the anatase-to-rutile phase transformation was observed.[38] As shown in the inset in Figure 2b, the position of the CeO_2 main peak (111) shifted to the left ($2\theta = 28.75°-28.67°$), indicating modification of the cell parameters. It is a widely reported fact in the literature that, during thermal treatments, a progressive depletion of oxygen occurs from the CeO_2 lattice, leading to the formation of sub-stoichiometric fluorite-structured CeO_{2-x}. Daushter et al., in their study on CeO_2-TiO_2 systems, reported the presence of oxygen vacancies.[39] The shift in the position of diffraction lines toward lower 2θ values originates from the presence of Ce^{3+} ions in the CeO_2 lattice. Because of the large difference between the ionic dimensions of the Ce^{4+} (0.97 Å) and Ce^{3+} (1.03 Å) ions, the lattice expansion of CeO_2 can be expected. This aspect has been elaborated in the subsequent paragraphs.

The powder XRD patterns of the CeO_2-ZrO_2 sample (CZ) calcined at 773 and 1073 K are shown in Figure 2c. As can be noted from this figure, the CeO_2-ZrO_2 calcined at 773 K exhibits poor crystallinity. Only the broad diffraction lines due to cubic fluorite-type phase with the composition $Ce_{0.75}Zr_{0.25}O_2$ (ICDD PDF No. 28-0271) are visible. With increasing calcination temperature, an increase in the intensity of the lines, because of better crystallization of this phase, could be noted. A slight shift in the peak positions ($2\theta = 28.90°-29.32°$) with increasing calcination temperature can be observed, which indicates that, along with particle growth, some compositional changes are also occurring. This is primarily due to a progressive increase of ZrO_2 content into the CeO_2 unit cell, because the ionic radius of zirconium (0.84 Å) is smaller than that of cerium (0.97 Å).[9] The observed additional broad diffraction patterns at higher calcination temperatures could be assigned to the $Ce_{0.6}Zr_{0.4}O_2$ phase (ICDD PDF No. 38-1439). Recently, Kenevey et al. reported the phase segregation phenomenon, which is considered to be surface-energy-driven, where the solid solutions are stable as long as the crystallite size does not exceed a critical size, above which the surface energy contribution to the total energy of the system is too small to allow its stabilization, thereby leading to the phase segregation.[40] Within the detection limits of the XRD technique, there is no evidence about the presence of tetragonal or monoclinic ZrO_2 (t-ZrO_2 or m-ZrO_2, respectively) phases.

Crystallite sizes (D_{XRD}) of CeO_2 in the CeO_2-SiO_2 and CeO_2-TiO_2 samples, and $Ce_{0.75}Zr_{0.25}O_2$ in CeO_2-ZrO_2, as a function of calcination temperature, are summarized in Table 1. Table 1 shows that the CeO_2 crystallization apparently is dependent on both the calcination temperature and the type of foreign cation present. Thus, the type of foreign cation and its concentration are crucial factors in modifying the thermal, textural, and redox properties of CeO_2. Selection of a suitable preparative analogy is also very important in creating a viable material. An increase in the crystallite size of CeO_2 is observed with increasing calcination temperature, with the increase being greater in the case of the Ce-Ti samples. The phenomenon of crystallite growth can be explained variously in each individual system. The coprecipitation of CeO_2, along with colloidal silica, could yield smaller crystallites of CeO_2 on the surface of SiO_2, which could coalesce under the impact of calcination, thus

TABLE 1: BET Surface Area and Crystallite Size Measurements of CeO_2 and $Ce_{0.75}Zr_{0.25}O_2$ in Various CeO_2-MO_2 (M = Si^{4+}, Ti^{4+}, and Zr^{4+}) Samples Calcined at Different Temperatures

calcination temperature (K)	surface area (m²/g cat.)	crystallite size (nm)
CeO_2-SiO_2 (1:1)		
773	147	3.2[a]
873	104	3.6[a]
973	75	4.4[a]
1073	54	6.0[a]
CeO_2-TiO_2 (1:1)		
773	59	10.0[a]
873	51	10.7[a]
973	42	11.8[a]
1073	31	14.1[a]
CeO_2-ZrO_2 (1:1)		
773	84	4.7[b]
873	67	4.8[b]
973	51	5.0[b]
1073	36	5.5[b]

[a] CeO_2. [b] $Ce_{0.75}Zr_{0.25}O_2$.
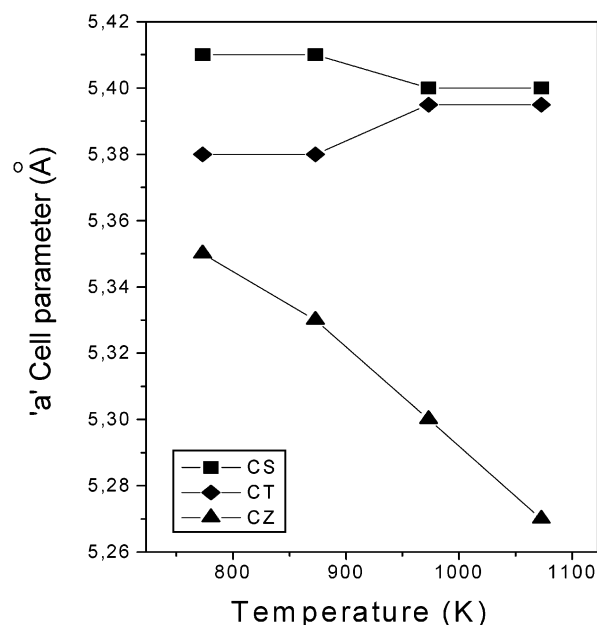
Figure 3. Cell parameter a measurements of various CeO_2-MO_2 (M = (■) Si^{4+} (CS), (◆) Ti^{4+} (CT), and (▲) Zr^{4+} (CZ)) binary oxides calcined at different temperatures.

accounting for an increase in the crystallite size. In the case of the Ce-Ti system, no tetragonalization of CeO_2 could be noted; the cubic CeO_2 structure prevailed, along with TiO_2 (anatase) modification. In particular, the Ce-Ti combination exhibited well-crystallized patterns with bigger crystallites within the realm of cubic modification. The formation of a solid solution between cerium and zirconium retards the crystallite growth, thus paving the way for the formation of thermodynamically more-stable phases.

Using the most intense (111) line of the CeO_2 and $Ce_{0.75}$-$Zr_{0.25}O_2$ patterns, cubic indexation and calculation of the unit-cell parameters have been conducted.[30,31] The evolution of cell parameter a values, as a function of the calcination temperature, is shown in Figure 3. The lattice parameters were estimated to determine whether the foreign cation enters into the CeO_2 lattice, resulting in the formation of a solid solution, or remains as a separate phase demarcated by a phase boundary. In some instances, incorporation may also occur; i.e., the foreign cation

can enter into the CeO$_2$ lattice without disturbing any of the neighboring Ce centers. In the case of the CeO$_2$−SiO$_2$ system, the *a* values obtained at various calcination temperatures are in good agreement with the pure CeO$_2$ (100%) phase.[31] However, a slight decline in the *a* values can be observed at higher calcination temperatures, which could be attributed to some incorporation of Si^{4+} cations (0.42 Å) into the CeO$_2$ lattice. Apparently, the CeO$_2$−SiO$_2$ binary oxide is characterized by the presence of small crystallites of CeO$_2$ on the surface of SiO$_2$. Interestingly, in the case of the CeO$_2$−TiO$_2$ system, a steady increase in the lattice parameters with increasing calcination temperature can be observed. The lattice expansion could be induced by the incorporation of Ti^{4+} cations into the CeO$_2$ lattice without disturbing the Ce centers, however, adopting different bonding positions, which lead to nonequivalent metal−oxygen distances. Note that the Ti^{4+} ionic radius (0.64 Å) is smaller than that of the Ce^{4+} cation (0.97 Å). The other possibility that could be responsible for the lattice expansion is the formation of oxygen vacancies. Under the impact of calcination treatment or dopant-induced defects, a depletion of oxygen occurs, leading to the formation of substoichiometric fluorite-structured CeO$_{2−x}$. Correspondingly, Ce^{3+} ions (1.03 Å) are formed, whose ionic radius is larger than that of Ce^{4+} ions (0.97 Å). As shown in the inset of Figure 2b, a noticeable shift in the positions of all peaks toward lower 2θ values could be taken as an indication of lattice expansion. More conclusively, the formation of oxygen vacancies due to various reasons (previously detailed) has a vital role in the expansion of the CeO$_2$ lattice. In the case of the CeO$_2$−ZrO$_2$ samples, there is a steady decrease in the lattice parameters with increasing calcination temperature. This observation can be attributed to shrinkage of the lattice, because of the replacement of Ce^{4+} ions (0.97 Å) with smaller Zr^{4+} cations (0.84 Å), in agreement with Vegard's law.[41,42] The progressive decrease in the lattice parameters can also be considered as evidence for incremental enrichment of the zirconium content into the cerium lattice. Overall, the lattice parameters of the presently studied binary oxides are well in the range of 5−6 Å and are in good agreement with earlier reports.[30,31] According to the literature, the Zr−O bond length in cubic ZrO$_2$ is 2.21 Å, which is much shorter than the Ce−O bond length in cubic CeO$_2$ (2.36 Å).[43] Thus, when Zr substitutes for Ce centers in the cubic fluorite lattice, two possibilities can be expected: (i) the Zr atoms may be forced into positions where metal−oxygen bond distances are much larger than those observed in pure ZrO$_2$, which, in turn, leads to an effective reduction in the oxidation state of Zr; or (ii) shrinkage of the lattice may occur, because of nonequivalent metal−oxygen bond lengths and different bonding positions.[43] On the basis of the information obtained from cell parameter *a* estimations and XPS measurements (Zr is in the highest oxidation state, Zr^{4+}, which will be addressed in the latter paragraphs; see later discussion), it can be inferred that lattice contraction is occurring.

The N$_2$ BET surface areas of various CeO$_2$−MO$_2$ (M = Si^{4+}, Ti^{4+}, and Zr^{4+}) mixed oxides calcined at different temperatures are presented in Table 1. The 773 K calcined samples exhibit reasonably high surface areas. However, the decrease is enormous after calcination at 1073 K, and the loss varies between 63% and 48%, depending on the sample under consideration. The observed decrease in the surface area with increasing calcination temperature could be attributed to better crystallization of CeO$_2$ and the formation of mixed phases. In particular, the CeO$_2$−SiO$_2$ combination showed a high surface area among other samples, because SiO$_2$ is well-known to be an effective surface area stabilizing agent for CeO$_2$. The

efficiency of foreign cations, in regard to preventing a loss of surface area at higher temperatures, seems to be related to the variations in the rate of crystal growth. The nature and concentration of foreign cations present in the system govern this variation.[13] Of course, there are two modes by which the decrease in surface area can be explained, namely grain-boundary formation and/or crystallite growth.[40] The present results indicate that, in the case of the CeO$_2$−SiO$_2$ binary oxide, the smaller crystallites that are formed at low calcination temperatures (Table 1) come together and coalesce, resulting in larger crystallites at higher calcination temperatures, thereby accounting for the decrease in the surface area. In the case of the CeO$_2$−TiO$_2$ binary oxide, a similar argument can be used to explain the decrease in the surface area and increase in the crystallite size at higher calcination temperatures. However, in the case of CeO$_2$−ZrO$_2$, the formation of solid solutions is responsible for the observed changes. The formation of newer, thermodynamically more stable phases and the appearance of well-demarcated grain boundaries between them lead to the decrease in surface area and subsequent crystallite growth. However, random replacement of Ce centers with Zr in a solid solution leads to structural perturbations in the lattice of the CeO$_2$, thereby interfering in the rate of normal crystallite growth and, thus, to some extent, ceasing the crystallite coalescence and the decline in the surface area.

In contrast to XRD results, which yield information related to the cation sublattice, Raman spectroscopy of these fluorite-type oxide structures are dominated by oxygen lattice vibrations, which are sensitive to the crystal symmetry, thus being a potential tool to obtain additional structural information. The Raman spectra of various binary oxides prepared in this study are shown in Figure 4. In general, the Raman spectra of CeO$_2$ is characterized by a strong band at 462 cm^{-1} that is due to the F$_{2g}$ Raman active mode of the fluorite structure.[44] In addition, it exhibits a weak band at ∼260 cm^{-1} and a shoulder at ∼600 cm^{-1}, which have been attributed, respectively, to the normal Raman inactive (IR active) transverse and longitudinal optical phonon modes at the Brillouin zone center.[45] As shown in Figure 4a, the Raman spectrum of CeO$_2$−SiO$_2$ calcined at 773 K shows a prominent peak at ∼457 cm^{-1} and a weak band at 600 cm^{-1}. The band at ∼457 cm^{-1} corresponds to the triply degenerate F$_{2g}$ mode and can be viewed as a symmetric breathing mode of the O atoms around Ce ions.[46] As the calcination temperature increased from 773 to 1073 K, the band at ∼457 cm^{-1} has been shifted to ∼461 cm^{-1}, sharpened, and become more symmetrical. This could be due to better crystallization of CeO$_2$ at higher calcination temperatures, as observed from XRD measurements. It is a known fact in the literature that the intensity of the Raman band is dependent on several factors, including the grain size and morphology. In general, inhomogeneous strain and phonon confinement are responsible for the broad and asymmetric character of the bands as the particle size gets smaller at lower calcination temperatures.[47] The weak band observed near 600 cm^{-1} could correspond to a nondegenerate longitudinal optical (LO) mode of CeO$_2$.[46,48] Normally, this mode should not be observed by RS; however, the presence of some defects can involve relaxation of the selection rules. In particular, this band has been linked to oxygen vacancies in the CeO$_2$ lattice.[49] This peak was observed in the case of nanosized samples and its relative intensity increased as the particle size gets smaller.[46] The same phenomenon is apparent in the present study. For each sample, the spectra were recorded at several points and no shift in the band position or difference of width was noted. This observation reveals clearly that the
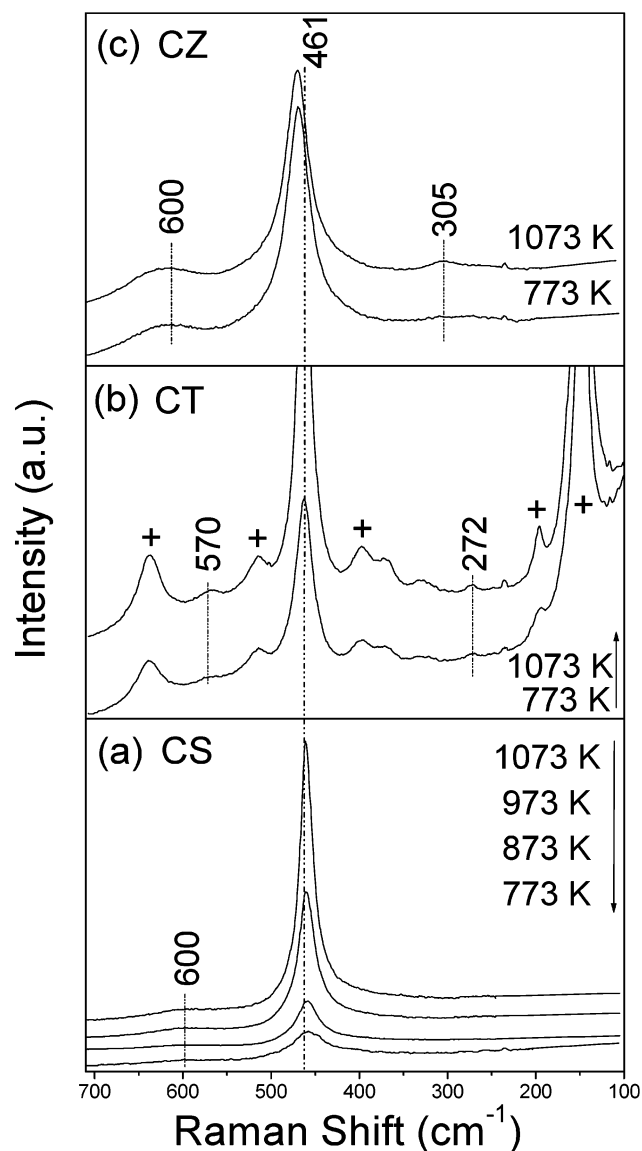
Figure 4. Raman spectra of various CeO_2-MO_2 (M = (a) Si^{4+} (CS), (b) Ti^{4+} (CT), and (c) Zr^{4+} (CZ)) binary oxides calcined at different temperatures. Cross symbol (+) denotes bands due to TiO_2 anatase.

CeO_2-SiO_2 sample is homogeneous. SiO_2 did not show any Raman features, as reported in the literature.[50] This gives an impression that SiO_2 forms a portion of the substrate support on which CeO_2 has been forming a surface overlayer. For very small crystallites (20–200 Å), the lack of long-range order relaxes the momentum conservation selection rule in the Raman scattering process. The Raman line shape in this case will be given by a weighted average of the phonon frequencies extending into the Brillouin zone, away from $q = 0$.[45] The result will be a shifted and broadened line shape. The broad band, reflecting the phonon density states, is a characteristic of Raman scattering from amorphous materials. Similar observations were made in the present study as expected and could be attributed to the method of preparation adopted. The absence of any other Raman features provides one more inference that SiO_2 is not forming any compound with cerium oxide, which is consistent with XRD measurements.

As presented in Figure 4b, the Raman spectrum of the CeO_2-TiO_2 sample calcined at 773 K shows a typical spectra of TiO_2 (anatase) (space group $I4_1/amd$)[36] and CeO_2.[46] The Raman bands pertaining to the TiO_2 (anatase) phase appear at 147, 196, 397,

514, and 638 cm^{-1}, whereas CeO_2 exhibits peaks at 272, 463, and 570 cm^{-1}, which are in agreement with the literature reports.[46] McBride et al. reported the Raman spectra of $Ce_{1-x}RE_xO_{2-y}$ (RE is a rare-earth element) solid solutions and found that the F_{2g} mode becomes asymmetric with the presence of a long, low-frequency tail as x increases, and there is also a weak shoulder on the high-frequency side of the band, which would evolve into a broad peak at ca. 570 cm^{-1} for larger values of x.[49] This broad peak is associated with oxygen vacancies in the solid solutions.[47,48] A similar phenomenon is apparent in the present study, which could be due to the incorporation of Ti^{4+} cations into the CeO_2 lattice at higher calcination temperatures. However, in agreement with XRD measurements, there is no evidence about the formation of detectable compounds between CeO_2 and TiO_2 from Raman results. Consistent with XRD results, there are a few extra broad Raman bands that could not be assigned to any of the known compounds. These could be due to Ce-Ti-O compounds whose presence must be established further. As shown in Figure 4c, the Raman spectrum of the CeO_2-ZrO_2 sample calcined at 773 K is dominated by a strong band at ~470 cm^{-1} and a less-prominent broad band at ~600 cm^{-1}. The band at ~470 cm^{-1} can be attributed to the F_{2g} vibration of the fluorite-type lattice. It is apparent from Raman results that the CeO_2-ZrO_2 support is mostly in the cubic form and does not show signs of tetragonal modification. The slight shift in the Raman frequency to higher wavenumbers could be due to a slight increase in the zirconium content into the CeO_2-ZrO_2 solid solution, as evidenced by XRD results. Thus, Raman results, to a certain extent, corroborate with the XRD results, signifying the enrichment of zirconium in a Ce–Zr solid solution at higher calcination temperatures. No Raman lines due to ZrO_2 could be observed, which is consistent with XRD measurements. According to literature, six Raman active modes ($A_{1g} + 3E_g + 2B_{1g}$) are expected for t-ZrO_2 (space group $P42/nmc$), whereas, for the cubic fluorite structure of CeO_2 (space group $Fm3m$), only one mode is Raman active.[17] As can be noted from Figure 4c, the peak at ~470 cm^{-1} becomes sharp as the calcination temperature increases, which could be due to better crystallization of the CeO_2-ZrO_2 solid solution at higher calcination temperatures, which is consistent with XRD measurements. It is quite obvious that sintering the samples at higher calcination temperatures increases the intensity of the F_{2g} band. It is also known that sintering the samples under high-temperature conditions leads to the formation of oxygen vacancies, which perturb the local M–O bond symmetry, leading to relaxation of the symmetry selection rules. The presence of a weak and less-prominent broad band near ~600 cm^{-1} is due to the LO mode of CeO_2, which occurs because of the relaxation of symmetry rules, as stated previously.[46,48] In particular, the substitution of ZrO_2 into the CeO_2 lattice, with an increase in temperature, results in oxygen vacancies, which are responsible for the emergence of this band.[49] The appearance of weak bands at ~300 and ~130 cm^{-1} (not shown in figure), at the calcination temperature of 1073 K, can be attributed to displacement of the O atoms from their ideal fluorite lattice position.[17]

To understand the nature of interactions between the host Ce ion and the foreign cations, the various binary oxides calcined at different temperatures were investigated by an XPS technique. The electron binding energies (in electron volts) of O 1s, Si 2p, Ti 2p, Zr 3d, and Ce 3d photoelectron peaks and the corresponding XPS atomic intensity ratios (Ce/Si, Ce/Ti, and Ce/Zr) are presented in Table 2. The electron binding energy values agree well with the literature reports.[32,33] Figure 5 displays

Structural Characterization of CeO_2-MO_2 Mixed Oxides

J. Phys. Chem. B, Vol. 107, No. 41, 2003 **11481**

TABLE 2: XPS Core-Level Binding Energies of Various CeO_2-MO_2 (M = Si^{4+}, Ti^{4+}, and Zr^{4+}) Samples Calcined at Different Temperatures

temperature (K)	Binding Energy (eV)					Ce/M atomic ratio, M = Si, Ti, Zr
	O 1s	Si $2p_{3/2}$	Ti $2p_{3/2}$	Zr $3d_{5/2}$	Ce $3d_{5/2}$	
			CeO_2-SiO_2			
773	530.1	103.7			881.7	0.71
873	530.2	103.6			881.3	0.70
973	530.2	103.8			881.3	0.71
1073	530.3	103.8			881.2	0.70
			CeO_2-TiO_2			
773	530.0		458.7		882.0	3.91
873	530.1		458.7		881.6	2.80
973	530.0		458.9		881.6	2.24
1073	530.3		459.1		881.8	1.85
			CeO_2-ZrO_2			
773	530.1			182.2	882.5	2.3
873	530.2			182.3	881.5	2.1
973	530.3			182.5	881.5	1.8
1073	530.3			182.6	881.3	1.6

the O 1s XP spectra of various mixed oxides investigated in this study. The O 1s peak is generally broad and complicated, because of the nonequivalence of surface O ions. As per the literature, the O ions in pure CeO_2 exhibit intense peaks at 528.6, 528.8, 529.6, and 530.1 eV, respectively.[25,51−53] The O 1s binding energy values reported for various other oxides, such as SiO_2,[25] TiO_2,[33,54] and ZrO_2,[55] are 532.7, 530.0, and 530.6 eV, respectively. The O 1s spectra (Figure 5) obtained for various samples are fairly similar, however, signifying the presence of modified CeO_2. Figure 5a represents the O 1s peaks of the CeO_2-SiO_2 sample calcined at 773 and 1073 K. As observed from this figure, the binding energy maxima of the most intense O 1s peak is almost constant at ∼530.1 eV, irrespective of the calcination temperature. Judging from the difference in the electronegativity of the Ce-metal system,[32,33] the SiO_2 contribution to the overall spectra is negligible, thus supporting the overlayer concept as envisaged previously.[26] The XPS is a well-known surface technique, with its attenuation depth of ∼20 Å. Thus, the XPS results are in agreement with the Raman measurements, giving the impression that CeO_2 overshadows the SiO_2 surface. Figure 5b represents the O 1s peaks of the CeO_2-TiO_2 sample. The O 1s peak of the sample calcined at 773 K shows a binding energy maximum at 530.0 eV that is due to the contribution from various oxide species in the sample. The shift and broadening of the peak toward higher binding energy can be attributed to a partial reduction of Ce^{4+} to Ce^{3+} under the conditions of XPS analysis, which is a well-documented fact in the literature. According to Paparazzo et al., sample evacuation under the condition of XPS analysis leads to partial reduction.[51] The appearance of Ce^{3+} ions at higher calcination temperatures was also confirmed from lattice parameter estimations, as envisaged previously. The appearance of Raman peak at ∼600 cm^{-1} also supported the presence of Ce^{3+} ions in the catalyst system. Figure 5c represents the O 1s peaks of the CeO_2-ZrO_2 binary oxide calcined at 773 and 1073 K. The binding energy of the most intense O 1s peak is observed at 530.1 eV, which can be attributed to the O atoms bound to $Ce_{0.75}Zr_{0.25}O_2$ solid solution, judging from the difference in the electronegativity of the constituent oxides involved.[32,33] The broadening of the peak and slight increase in the binding energy values, because of the greater electronegativity of the zirconium, with increasing calcination temperature, can be considered as evidence for the surface enrichment of zirconium into the CeO_2 lattice and subsequent appearance of the $Ce_{0.6}Zr_{0.4}O_2$ phase.

The binding energy of the Si 2p peak (figure not shown), in the case of the CeO_2-SiO_2 binary oxide, was 103.6−104.0 eV, which agree well with the values reported in the literature.[25,56,57] The poor intensity of the spectra with a large peak width indicates that the silica surface is not easily accessible at the surface, because of the presence of the CeO_2 overlayer. The Ti 2p photoemission spectra (figure not shown) of the CeO_2-TiO_2 binary oxide exhibited typical peaks in the range of 458.7−459.1 eV for Ti $2p_{3/2}$, which are in agreement with previous reports.[54,58,59] The intensity of the Ti 2p core-level spectra increased as the calcination temperature increased, because of better crystallization of TiO_2. The core-level spectra of Zr 3d (figure not shown), in the case of the CeO_2-ZrO_2 binary oxide, showed progressive broadening, along with a shift toward higher binding energy—from 182.2 eV to 182.6 eV—with increasing calcination temperature, indicating the formation of solid solutions between CeO_2 and ZrO_2 in different stoichiometric combinations, as envisaged previously. The slight increase in the binding energy of the Zr 3d photoelectron peak with increasing calcination temperature (Table 2), however (within the range of 182.2−182.6 eV), is in agreement with the values reported in the literature and supports the formation of the $Ce_{0.75}Zr_{0.25}O_2$ phase at lower calcination temperatures.[18,32,33,55] A slight shift toward higher binding energy with increasing calcination temperature also signifies the surface enrichment of zirconium and subsequent formation of the $Ce_{0.6}Zr_{0.4}O_2$ phase, as mentioned previously. The XPS studies indicate that all constituent oxides in the CeO_2-MO_2 (M = Si, Ti, and Zr) mixed oxides are present in their highest oxidation states (Si^{4+}, Ti^{4+}, and Zr^{4+}) and show no sign of reduction under the conditions used in this study.

The CeO_2 3d photoelectron peaks of various CeO_2-MO_2 binary oxide samples used in this study are shown in Figure 6. The assignment of CeO_2 3d photoelectron peaks is ambiguous, because of the complex nature of the spectra, which occurs not only because of multiple oxidation states but also because of the mixing of Ce 4f levels and O 2p states during the primary photoemission process.[25] This hybridization leads to multiplet splitting of the peaks into doublets, with each doublet showing further structure that is due to final state effects.[60,61] On the basis of the works of Burroughs et al.,[62] Pfau and Schierbaum,[53] and Creaser et al.,[63] the Ce 3d spectrum can be assigned as follows. Two sets of spin−orbital multiplets, corresponding to the $3d_{3/2}$ and $3d_{5/2}$ contributions, are labeled as u and v, respectively. The peaks labeled v and v″ have been assigned to a mixing of the Ce $3d^9$ $4f^2$ O $2p^4$ and Ce $3d^9$ $4f^1$ O $2p^5$ Ce(IV) final states, and the peak denoted v‴ corresponds to the Ce $3d^9$ $4f^0$ O $2p^6$ Ce(IV) final state. On the other hand, lines v_0 and v′ are assigned to the Ce $3d^9$ $4f^2$ O $2p^5$ and Ce $3d^9$ $4f^1$ O $2p^6$ states of Ce(III). The same assignment can be applied to the u structures, which correspond to the Ce $3d_{3/2}$ levels. As shown in Figure 6a, the XP spectrum of the CeO_2-SiO_2 sample calcined at 773 K exhibits peaks that are due to the presence of both Ce^{4+} and Ce^{3+} ions, thus implying that cerium is present at the surface in both 4+ and 3+ oxidation states. With increasing calcination temperature, the relative intensity of u′ and v′ annotated peaks increased, indicating an increase in the surface content of Ce^{3+} ions. The Ce^{3+} ions probably have been formed due to the reduction of CeO_2 under the conditions of ultrahigh-vacuum treatment during XPS measurements.[51,64,65] However, the presence of Ce_2O_3 was not observed from XRD measurements. As shown in Figure 6b, the Ce 3d spectrum of the CeO_2-TiO_2 sample basically denotes a mixture of Ce^{3+}/Ce^{4+} oxidation states, resulting in a myriad of peaks, indicating
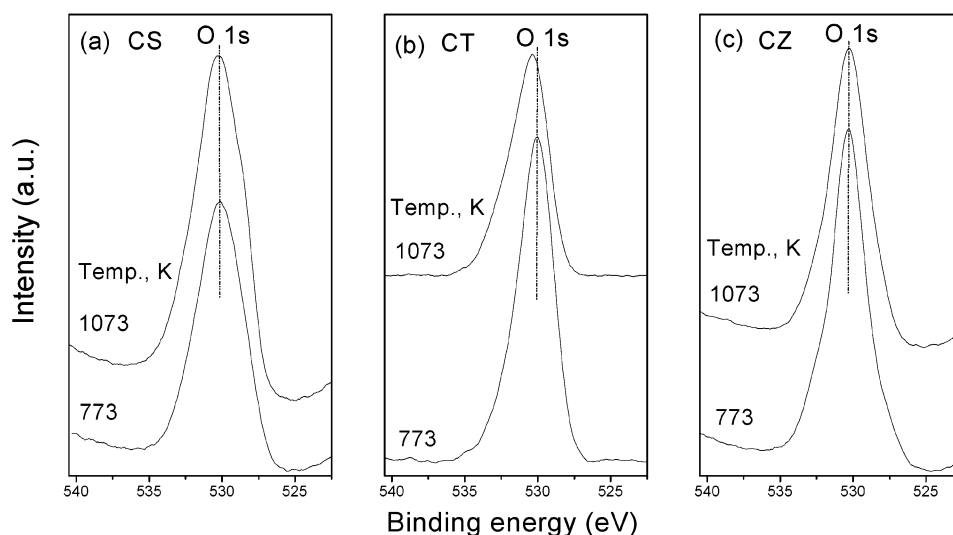
Figure 5. O 1s XPS spectra of various CeO_2-MO_2 (M = (a) Si^{4+} (CS), (b) Ti^{4+} (CT), and (c) Zr^{4+} (CZ)) binary oxides calcined at different temperatures.

Figure 6. Ce 3d XPS spectra of various CeO_2-MO_2 (M = (a) Si^{4+} (CS), (b) Ti^{4+} (CT), and (c) Zr^{4+} (CZ)) binary oxides calcined at different temperatures.
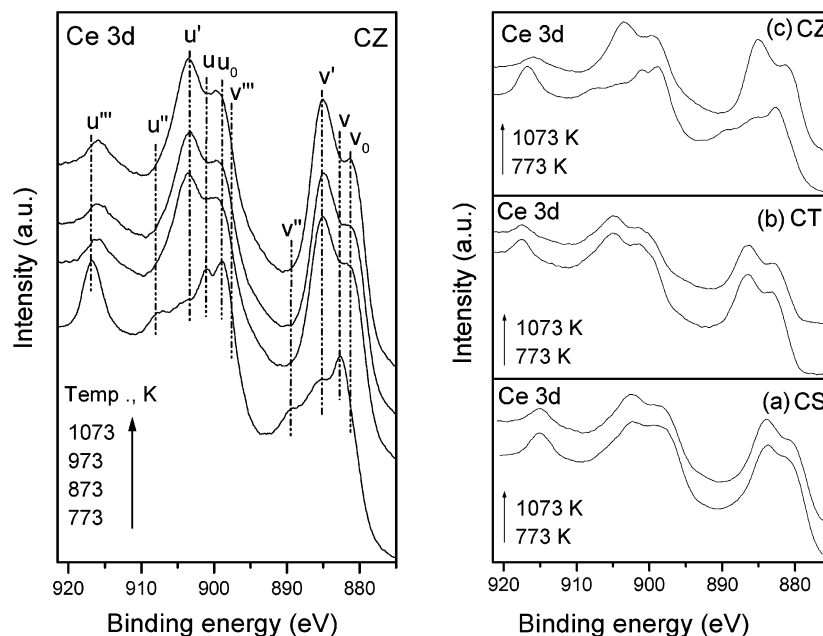
that the surface of the sample is not fully oxidized. With increasing calcination temperature, the intensity of the u'/v' doublet due to primary photoemission from the Ce^{3+} ion, relative to the intensities of the peaks due to photoemission from the Ce^{4+} ion (i.e., u/v, u''/v'', and u'''/v''') increased gradually up to 873 K and then decreased. An additional peak centered at 880.9 eV was observed in the spectrum.[23] This peak is a shakedown feature resulting from a filled O 2p orbital to a Ce 4f orbital during photoemission from Ce^{3+} cations. This shakedown feature results in an additional doublet, which is labeled as u_0/v_0 in the spectrum. The presence of u_0/v_0 and u'/ v' doublet peaks indicates that the CeO_2-TiO_2 sample contains some oxygen vacancies and is in a partially reduced state. The change in the intensity of the primary photoemission peaks from Ce^{4+} cations (i.e., u/v, u''/v'', and u'''/v''') with increasing calcination temperature could be due to the partial incorporation of Ti^{4+} ions into the CeO_2 lattice, which is consistent with RS measurements. A partial photo reduction of CeO_2 during XPS measurements is also a well-known fact in the literature.[51,64,65]

The reduction is mainly due to the progressive elimination of surface hydroxyls and O ions from the CeO_2 surface upon vacuum treatment. Figure 6c represents the XP spectra of the CeO_2-ZrO_2 binary oxide calcined at 773 and 1073 K. The 773 K calcined sample apparently shows a typical peak shape that corresponds to the Ce(IV) oxidation state. As the calcination temperature increases, the structures due to v, v'', v''', and u and u'' disappear progressively and the intensity of the u''' peak decreases. At higher calcination temperatures, the intensity of structures due to u_0, v_0, u', and v' increased, indicating an increase in the surface content of Ce(III) ions. As mentioned previously, the reduction of the Ce(IV) ion under the conditions of ultrahigh vacuum during XPS measurements could lead to the formation of Ce(III) ions. However, XRD could not detect any visible Ce_2O_3 lines. Thus, the XPS studies, up to a certain extent, corroborate with the XRD and Raman measurements.

The Ce/M (M = Si, Ti, or Zr) atomic ratios, as determined by XPS, are presented in Table 2. As observed from Table 2, the Ce/Si atomic ratios in various CeO_2-SiO_2 samples are fairly

Structural Characterization of CeO₂−MO₂ Mixed Oxides

J. Phys. Chem. B, Vol. 107, No. 41, 2003 **11483**

constant, irrespective of the calcination temperature, thus signifying the fact that CeO_2 crystallites are stabilized over the surface of the SiO_2 support and the entire system is thermodynamically stable. The Ce/Ti atomic ratios decrease, as a function of the calcination temperature, and the decrease can be attributed to the incorporation of Ti^{4+} cations into the CeO_2 lattice, thereby increasing the surface content of Ti^{4+} ions at higher calcination temperatures, as evidenced earlier by the estimations of cell parameter a. In the case of the CeO_2-ZrO_2 sample, the Ce/Zr atomic ratios decrease as the calcination temperature increases, thus supporting the surface enrichment of ZrO_2 that is due to the formation of a zirconium-rich $Ce_{0.6}Zr_{0.4}O_2$ phase over the surface. Thus, the XPS atomic ratio information further supports the conclusions drawn from XRD and Raman techniques.

4. Conclusions

(1) By adopting coprecipitation or deposition precipitation methodologies, the preparation of 1:1 molar ratio binary oxides of CeO_2-MO_2 (M = Si^{4+}, Ti^{4+}, and Zr^{4+}) were undertaken. These preparations yield fairly homogeneous and stable mixed oxides with reasonably high specific surface areas.

(2) The effect of foreign cations on the crystal modification of the CeO_2 cubic lattice was mainly focused. All the binary oxides investigated in this study predominantly exhibit CeO_2 cubic modification. The cubic structure is more favored, because the tetragonal structure is rather inactive in catalysis.

(3) The CeO_2-SiO_2 sample exhibited relatively small crystallites of CeO_2 over the surface of the SiO_2 substrate, whereas the CeO_2-TiO_2 sample was comprised of large crystallites of CeO_2.

(4) The measurement of values of cell parameter a, using the cubic indexation method, was performed. The results suggest some incorporation of Si^{4+} ions into the CeO_2 lattice at higher calcinations temperatures, in the case of the CeO_2-SiO_2 samples. An expansion and contraction of the CeO_2 lattice were noted in the case of the CeO_2-TiO_2 and CeO_2-ZrO_2 samples, respectively.

(5) Raman measurement provided considerable information on the fluorite structure of CeO_2. In particular, displacement of the oxygen sublattice in the fluorite structure and the presence of oxygen vacancies/Ce^{3+} ions were noted in the case of the CeO_2-TiO_2 and CeO_2-ZrO_2 samples.

(6) The XPS measurements showed that various binary oxide constituents are in their highest oxidation states: Si^{4+}, Ti^{4+}, and Zr^{4+}. Cerium displays the presence of both Ce^{4+} and Ce^{3+} oxidation states, however, in different proportions, depending on the nature of the binary oxide system and the calcination temperature used.

References and Notes

(1) Bernal, S.; Kasper, J.; Trovaralli, A. Recent Progress in Catalysis by Ceria and Related Compounds. *Catal. Today* **1999**, *50*, 173.

(2) Sato, T.; Dosaka, K.; Ishitsuka, M.; Haga, E. M.; Okuwaki, A. *J. Alloys Compd.* **1993**, *193*, 274.

(3) Sahibzada, M.; Steele, B. C. H.; Zheng, K.; Rudkin, R. A.; Metcalfe, I. S. *Catal. Today* **1997**, *38*, 459.

(4) Rossignol, S.; Madier, Y.; Duprez, D. *Catal. Today* **1999**, *50*, 261.

(5) Fornasiero, P.; Balducci, G.; Di Monte, R.; Kaspar, J.; Sergo, V.; Gubitosa, G.; Ferrero, A.; Graziani, M. *J. Catal.* **1995**, *164*, 173.

(6) Fornasiero, P.; Di Monte, R.; Rao, G. R.; Kaspar, J.; Meriani, S.; Trovarelli, A.; Graziani, M. *J. Catal.* **1995**, *151*, 168.

(7) Trovarelli, A. *Catal. Rev. Sci. Eng.* **1996**, *38*, 439 and references therein.

(8) Trovarelli, A. *Commun. Inorg. Chem.* **1999**, *20*, 263.

(9) Trovarelli, A.; de Leitenburg, C.; Dolcetti, G. *CHEMTECH* **1997**, *27*, 32.

(10) Taylor, K. C. *Catalysis Science and Technology*; Springer−Verlag: Berlin, 1984; Chapter 2.

(11) Qi, G.; Yang, R. T. *J. Chem. Soc. Chem. Commun.* **2003**, 848.

(12) Schmieg, S. J.; Belton, D. N. *Appl. Catal. B: Environ.* **1995**, *6*, 127.

(13) Trovarelli, A.; Boaro, M.; Rocchini, E.; de Leitenburg, C.; Dolcetti, G. *J. Alloys Compd.* **2001**, *323*, 584.

(14) Ozawa, M.; Kimura, M.; Sobukawa, H.; Yokota, K. *Toyota Tech. Rev.* **1992**, *27*, 43.

(15) Mikki, T.; Ogawa, T.; Haneda, M.; Kakuta, N.; Ueno, A.; Tateishi, S.; Maysuura, S.; Sato, M. *J. Phys. Chem.* **1990**, *94*, 6464.

(16) Shuk, P.; Greenblatt, M.; Croft, M. *Chem. Mater.* **1999**, *11*, 473.

(17) Yashima, M.; Arashi, H.; Kakihana, M.; Yoshimura, M. *J. Am. Ceram. Soc.* **1994**, *77*, 1067.

(18) Reddy, B. M.; Khan, A.; Yamada, Y.; Kobayashi, T.; Loridant, S.; Volta, J. C. *Langmuir* **2003**, *19*, 3025.

(19) Zhang, Y.; Andersson, A.; Muhammed, M. *Appl. Catal. B: Environ.* **1995**, *6*, 325.

(20) Lammonier, C.; Bennani, A.; D'Huysser, A.; Aboukais, A.; Wrobel, G. *J. Chem. Soc., Faraday Trans.* **1996**, *92*, 131.

(21) Imamura, S.; Shono, M.; Okamoto, N.; Haneda, A.; Ishida, S. *Appl. Catal. A: General* **1996**, *142*, 279.

(22) Rynkowski, J.; Farbotko, J.; Touroude, R.; Hilaire, L. *Appl. Catal. A: General* **2000**, *203*, 335.

(23) Reddy, B. M.; Khan, A.; Yamada, Y.; Kobayashi, T.; Loridant, S.; Volta, J. C. *J. Phys. Chem. B* **2003**, *107*, 5162.

(24) Usmen, R. K.; Graham, G. W.; Watkins, W. L. H.; McCabe, R. W. *Catal. Lett.* **1995**, *30*, 53.

(25) Bensalem, A.; Bozon-Verduraz, F.; Delamar, M.; Bugli, G. *Appl. Catal. A: General* **1995**, *121*, 81.

(26) Reddy, B. M.; Khan, A.; Yamada, Y.; Kobayashi, T.; Loridant, S.; Volta, J. C. *J. Phys. Chem. B* **2002**, *106*, 10964.

(27) Liu, W.; Flytzani-Stephanopoulos, M. *J. Catal.* **1995**, *153*, 304.

(28) Preuss, A.; Gruehn, R. *J. Solid State Chem.* **1994**, *110*, 363.

(29) Klug, H. P.; Alexander, L. E. *X-ray Diffraction Procedures for Polycrystalline and Amorphous Materials*, 2nd ed.; Wiley: New York, 1974.

(30) Bozo, C.; Gaillard, F.; Guilhaume, N. *Appl. Catal. A: General* **2001**, *220*, 69.

(31) Colon, G.; Pijolat, M.; Valdivieso, F.; Vidal, H.; Kaspar, J.; Finocchio, E.; Daturi, M.; Binet, C.; Lavalley, J. C.; Baker, R. T.; Bernal, S. *J. Chem. Soc., Faraday Trans.* **1998**, *94*, 3717.

(32) Briggs, D., Seah, M. P., Eds. *Practical Surface Analysis*, 2nd ed.; Auger and X-Ray Photoelectron Spectroscopy; Wiley: New York, 1990; Vol. 1.

(33) Wagner, C. D.; Riggs, W. M.; Davis, L. E.; Moulder, J. F. In *Handbook of X-ray Photoelectron Spectroscopy*; Muilenberg, G. E., Ed.; Perkin−Elmer Corporation: Eden Prairie, MN, 1978.

(34) Rocchini, E.; Trovarelli, A.; Llorca, J.; Graham, G. W.; Weber, W. H.; Maciejewski, M.; Baiker, A. *J. Catal.* **2000**, *194*, 461.

(35) Rocchini, E.; Vicario, M.; Llorca, J.; de Leitenburg, C.; Dolcetti, G.; Trovarelli, A. *J. Catal.* **2002**, *211*, 407.

(36) Hadjiivanov, K. I.; Klissurski, D. G. *Chem. Soc. Rev.* **1996**, *25*, 61 and references therein.

(37) Lin, J.; Yu, J. C. *J. Photochem. Photobiol. A: Chem.* **1998**, *116*, 63.

(38) Anderson, C.; Bard, A. J. *J. Phys. Chem.* **1994**, *98*, 1769.

(39) Dauscher, A.; Hilaire, L.; Le Normand, F.; Muller, W.; Maire, G.; Vasquez, A. *Surf. Interface Anal.* **1990**, *16*, 341.

(40) Kenevey, K.; Valdivieso, F.; Soustelle, M.; Pijolat, M. *Appl. Catal. B: Environ.* **2001**, *29*, 93.

(41) Shannon, R. D. *Acta Crystallogr., Sect. A: Cryst. Phys., Diffr., Theor. Gen. Crystallogr.* **1976**, *32*, 751.

(42) Meriani, S.; Spinolo, G. *Powder Diffr.* **1987**, *2*, 255.

(43) Liu, G.; Rodriguez, J. A.; Hrbek, J.; Dvorak, J.; Peden, C. H. F. *J. Phys. Chem. B* **2001**, *105*, 7762.

(44) Martinez-Arias, A.; Fernandez-Garcia, M.; Salamanca, L. N.; Valenzuela, R. X.; Conesa, J. C.; Soria, J. *J. Phys. Chem. B* **2000**, *104*, 4038.

(45) Shyu, J. Z.; Weber, W. H.; Gandhi, H. S. *J. Phys. Chem.* **1988**, *92*, 4964.

(46) Lin, X.-M.; Li, L.-P.; Li, G.-S.; Su, W.-H. *Mater. Chem. Phys.* **2001**, *69*, 236.

(47) Spanier, J. E.; Robinson, R. D.; Zhang, F.; Chan, S.-W.; Herman, I. P. *Phys. Rev. B* **2001**, *64*, 245407.

(48) Weber, W. H.; Hass, K. C.; McBride, J. R. *Phys. Rev. B* **1993**, *48*, 178.

(49) McBride, J. R.; Hass, K. C.; Poindexter, B. D.; Weber, W. H. *J. Appl. Phys.* **1994**, *76*, 2435.

(50) Wachs, I. E.; Deo, G. *J. Phys. Chem.* **1991**, *95*, 5889.

(51) Paparazzo, E.; Ingo, G. M.; Zacchetti, N. *J. Vac. Sci. Technol. A* **1991**, *9*, 1416.

(52) Praline, G.; Koel, B. E.; Hance, R. L.; Lee, H.-I.; White, J. M. *J. Electron Spectrosc. Relat. Phenom.* **1980**, *21*, 71.

(53) Pfau, A.; Schierbaum, K. D. *Surf. Sci.* **1994**, *321*, 71.

(54) Biener, J.; Baumer, M.; Wang, J.; Madrix, R. J. *Surf. Sci.* **2000**, *450*, 12.

(55) Galtayries, A.; Sporken, R.; Riga, J.; Blanchard, G.; Caudano, R. *J. Electron Spectrosc. Relat. Phenom.* **1998**, *88−91,* 951.

(56) Reddy, B. M.; Ganesh, I.; Reddy, E. P. *J. Phys. Chem. B* **1997**, *101*, 1769.

(57) Bukhtiyarov, V. I. *Catal. Today* **2000**, *56*, 403.

(58) Wang, Q.; Madrix, R. J. *Surf. Sci.* **2001**, *474*, L213.

(59) Reddy, B. M.; Ganesh, I.; Reddy, E. P.; Fernández, A.; Smirniotis, P. G. *J. Phys. Chem. B* **2001**, *105*, 6227.

(60) Wong, G. S.; Vohs, J. M. *Surf. Sci.* **2002**, *498*, 266.

(61) Mullins, D. R.; Overbury, S. H.; Huntley, D. R. *Surf. Sci.* **1998**, *409*, 307.

(62) Burroughs, A.; Hamnett, A.; Orchard, A. F.; Thornton, G. *J. Chem. Soc., Dalton Trans.* **1976**, *1*, 1686.

(63) Creaser, D. A.; Harrison, P. G.; Morris, M. A.; Wolfindale, B. A. *Catal. Lett.* **1994**, *23*, 13.

(64) Park, P. W.; Ledford, J. S. *Langmuir* **1996**, *12*, 1794.

(65) Fierro, J. L. G.; Soria, J.; Sanz, J.; Rojo, J. M. *J. Solid State Chem.* **1987**, *66*, 154.